Journal of Materials Chemistry A

Accepted Manuscript

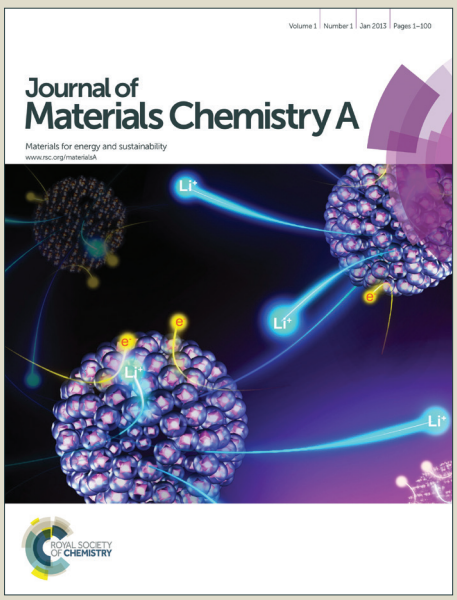

ROYAL SOCIETY OF CHEMISTRY

www.rsc.org/materialsA

Cite this: DOI: 10.1039/c0xx00000x

www.rsc.org/xxxxxx

ARTICLE TYPE

Synthesis of corundum type In_2O_3 porous spheres and their photocatalytic properties

Binglin Tao [a], Ying Zhang [*a], Dezhi Han [b], Yanpeng Li [a] and Zifeng Yan [*a]

Received (in XXX, XXX) Xth XXXXXXXXX 20XX, Accepted Xth XXXXXXXXX 20XX

DOI: 10.1039/b000000x

In this work, polycrystalline indium oxyhydroxide (InOOH) porous spheres were synthesized through a mixed solvothermal method in the presence of sodium citrate (Na_3cit) as the structure-directing agent. Corundum-type In_2O_3 porous spheres were obtained via annealing InOOH precursors at 400 °C for 2 hours. The samples were characterized by means of X-ray powder diffraction, thermogravimetric analysis, UV-Vis diffuse reflectance spectroscopy, scanning electron microscopy, transmission electron microscopy, and high-resolution transmission electron microscopy. Ostwald ripening process was proposed as the mechanism for the formation of porous spheres. Photocatalytic activity of the porous h-In_2O_3 spheres was evaluated by degrading rhodamine B (RhB) under ultraviolet (UV) irradiation. The results indicated that the porous h-In_2O_3 spheres possessed superior photocatalytic activity to their counterparts, and could restore 95% of the initial photocatalytic activity after 5 reaction runs.

Introduction

Till now, micro/nanoscale metal oxides with well-defined structures have received great attention in a myriad of research fields such as chemical sensors[1], photonic devices[2], drug-delivery carriers[3], field emission displays[4], photocatalysis[5], and lithium-ion batteries[6], owing to their unique morphologies and physicochemical properties which are different from their bulk counterparts. The physical and chemical properties of nanomaterials are strongly dependent on their particle size, porosity, specific surface area, structure and morphology. In order to obtain functional metal oxides materials with excellent performance, many efforts have been devoted to explore the preparation strategies in the past few decades. So far, a broad range of nanostructured metal oxides have been successfully synthesized by various methods including laser ablation[7], physical and chemical vapour deposition[8], hydrothermal[9] and solvothermal[10] methods, electrostatic spinning[11], and template-assisted[12] approaches.

As an n-type semiconductor with a direct band gap of 3.55-3.75 eV, indium oxide has been intensively investigated in recent years. Previous reports showed that In_2O_3 with different morphologies could be synthesized controllably, such as nanocubes[13], nanofibers[14], nanotubes[15], nanorods[16], nanosheets[13], 3D-urchins[17], flowers[18] and hierarchical spheres[19]. Normally, In_2O_3 prefers to crystallize in the form of cubic structure (c-In_2O_3), whereas metastable corundum-type In_2O_3 (h-In_2O_3) was obtained by phase transition method under high temperature and high pressure (HTHP) conditions[20, 21]. Over the past few years, rapid advances have been achieved for the fabrication of micro/nanostructured h-In_2O_3 in solvothermal systems. For example, h-In_2O_3 nanofibers with an interesting bamboo-like domain structure have been synthesized in the presence of ether[14]. Literature shows that the presence of water is detrimental to h-In_2O_3 precursors[22], there are very few reports focused on the synthesis of h-In_2O_3 by hydrothermal methods. In spite of the maturity characteristic of solvothermal methods, the toxicity, high cost, and operational risk necessitate the development of alternative way to synthesize h-In_2O_3 under water or water-solvent binary conditions. On the other hand, high energy consumption and pollution level of chemical vapour deposition based methods restrict their large scale fabrication. Thus it is urgent to develop a cheap and effective hydrothermal or mixed solvothermal method to prepare h-In_2O_3.

In this study, we propose a water-ethylene glycol binary solvent system for the synthesis of h-In_2O_3 porous spheres by annealing InOOH precursor at 400 °C for 2 hours under ambient pressure. The nucleus formation and subsequent ripening process result in the formation of porous spheres. Besides, these novel porous h-In_2O_3 spheres could be used to degrade RhB under UV illumination, showing their potential application in pollution abatement.

Experimental

Preparation of InOOH and h-In_2O_3

Indium chloride tetrahydrate and rhodamine B were purchased from Sigma-Aldrich. All the other reagents were acquired from Sinopharm Chemical Reagent Co., Ltd. (China), and used without further purification. In a typical synthesis, 0.293 g of $InCl_3$•$4H_2O$ was firstly dissolved in 60 mL of deionized water and ethylene glycol binary solvent (water: ethylene glycol=1:1). Subsequently, 0.96 g urea and 1.0 g of sodium citrate were added to the solution successively. Under vigorous stirring for 10 min, this transparent

solution was transferred to a 100 mL Teflon-lined stainless steel autoclave, which was sealed and then heated at 200 °C for 16 h. After cooling down to room temperature in air, the resulting grey white precipitates were centrifuged and washed with distilled water and absolute ethanol for 3 times, followed by drying at 80 °C for 6 h. H-In_2O_3 was obtained by annealing InOOH precursor at 400 °C for 2 h in a muffle furnace. To investigate the influence of reaction conditions on the products, samples with different water-ethylene glycol volume ratios, reaction temperatures and reaction times have been synthesized.

Characterization

X-ray powder diffraction (XRD) measurement was performed on a PANalytical X-ray Diffractometer equipped with Cu Kα radiation (λ=0.15406 nm, 40 kV, 40 mA). Thermal gravity analysis was collected on a Netzsch thermal gravimetric analyser under with the rate of 10 °C/min up to 700 °C in air atmosphere. Fourier transform infrared (FT-IR) spectra were recorded on a Nicolet 6700 spectrometer. Field emission scanning electron microscopy (FESEM) images were taken using a Hitachi S-4800 scanning electron microscope at an accelerating voltage of 5 kV. The transmission electron microscopy (TEM) images and selected area electron diffraction patterns were obtained by the JEOL JEM-2100UHR microscope with an accelerating voltage of 200 kV. Diffuse reflectance spectra were recorded on Jena SPECORD 210 PLUS UV-Vis spectrophotometer using $BaSO_4$ as the reference. Nitrogen sorption was performed on a Micromerities Tristar 3000 equipment at -196 °C, and the surface area was calculated by the BET method.

Photocatalytic Activity Test

The photocatalytic activity of the h-In_2O_3 porous spheres was evaluated by degrading RhB under UV irradiation. A lab-made 300 mL quartz beaker was used as the reactor. Typically, 50 mg of the as synthesized h-In_2O_3 spheres was added to 50 mL of 1×10^{-5} M RhB aqueous solution to form a suspension (1 mg/mL). After that, the reaction system was magnetically stirred for 30 min to establish adsorption-desorption equilibrium between the dye and catalysts. Then the reaction system was irradiated with a 250 W high pressure mercury lamp (the wavelength centered at 365 nm) which was placed 20 cm above the reactor. At a given irradiation interval of 30 min, 1.5 mL of solution was withdrawn from the reactor for analysis. The characteristic absorption peak of RhB at 554 nm was chosen for quantitatively determining the dye concentration, which is calculated from a predetermined 5-point calibration curve. Besides, deionized water was used as the reference. The absorption spectra were recorded by Jena SPECORD 210 PLUS UV-Vis spectrophotometer.

Results and Discussion

The XRD patterns of the as-synthesized InOOH precursors (water-ethylene glycol volume ratio: 30:30; temperature: 200 °C; reaction time: 16 h) are shown in Fig. 1a. Before annealing, all the diffraction peaks could be indexed as InOOH with orthorhombic structure (JCPDS No.71-2277). No impurity peaks were detected, indicating the high quality of the products. Fig. 1b shows the FT-IR spectrum of the InOOH precursor. The broad peak centered at 3403cm^{-1} and the small sharp peak centered at 1636cm^{-1} were ascribed to the O-H stretching and bending vibrations, respectively[23]. Two bands at 2972cm^{-1} and 2852cm^{-1} were attributed to the $-CH_2$ stretching modes, demonstrating the existence of Na_3cit residues. Two broad weak peaks at 2702cm^{-1} and 2004cm^{-1} are typical O-H vibrations of InOOH[24]. Also, the peaks of 1403cm^{-1}, 1271cm^{-1}, 1154cm^{-1} and 1048cm^{-1} were assigned to the O-H bending or deformation vibrations[25].

The morphology and structure of the InOOH precursor were demonstrated by FESEM and TEM. The low magnification SEM image indicates the products possess well-dispersed spherical structure with uniform diameter in the range of 600-700 nm (Fig. 1c&d). Fig. 1d reveals the rough surface of an isolated porous sphere. It is speculated that the architecture was composed of small nanoparticles with dimensional size from several ten nanometer to a hundred nanometer. Numerous 0D-nanoparticles arranged irregularly and self-assembled to form the porous structure. Low magnification TEM image of Fig. 1e displays that the InOOH precursors possess porous architecture due to the contrast between the dark circumference and the relatively bright center. The corresponding SAED pattern in Fig. 1f further confirms these hierarchical architectures are polycrystalline. These diffraction rings could be indexed as orthorhombic phase of InOOH and the relevant lattice planes were identified with the XRD analytical results. HRTEM images with distinct lattice fringes were hard to shoot, because the 3D-architectures were too thick for the electron to penetrate. Besides, the instability of the oxyhydroxide precursor under electron irradiation should also be responsible for the inferior quality of HRTEM images[26].

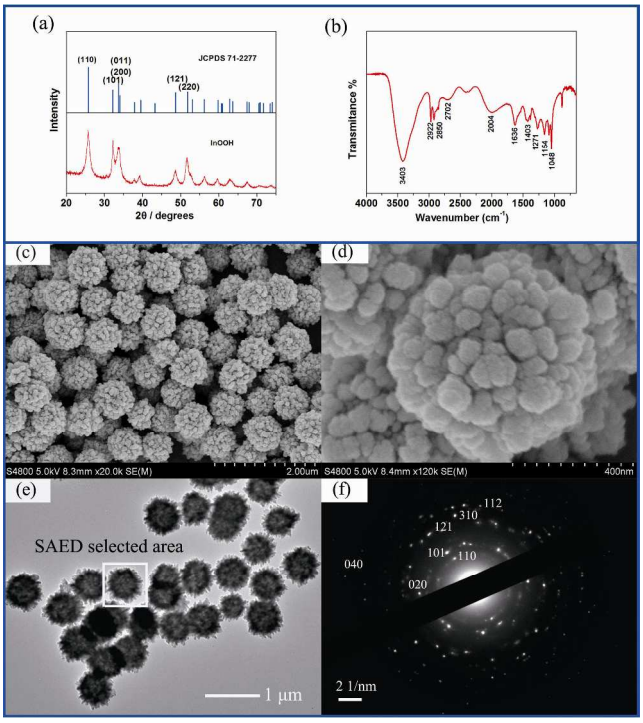

Figure 1. (a) XRD patterns of InOOH porous spheres and their corresponding JCPDS card; (b) FT-IR spectrum of the as-synthesized InOOH products; (c) Low and (d) high-magnification FESEM images of InOOH spheres; (e) low-magnification TEM image of InOOH spheres and (f) corresponding SEAD patterns of an isolated sphere. The sample was synthesized at a water-ethylene glycol volume ratio of 30:30, temperature of 200 °C and reaction time of 16 h.

Previous reports suggested that the solvent composition has a significant impact on the phase structure[27]. In this experiment, the influence of solvents on the products was investigated by changing the water-ethylene glycol volume ratios (W: E), while temperature and reaction time were kept at 200 °C and 16 h, respectively. Table 1 summarizes the morphologies and crystal structures of the products prepared at different water-ethylene glycol volume ratios. Particularly, once excessive amount of ethylene glycol was added into the binary system, no precipitation was formed. As shown in Fig. S2, when the water-ethylene glycol volume ratio was set at both 60:0 and 50:10, unconsolidated spheres with mixed crystal structures were obtained. When the products were prepared at a volume ratio of 40:20, considerable smooth spheres were obtained, which account for approximate 5% of the final products. As for the sample prepared at volume ratio of 20:40, only agglomerated co-crystalline particles could be obtained. The crystal structure variations (XRD spectra) and their corresponding SEM images under different solvent ratios (Fig. S1&S2) indicate that the solvent composition has little influence on the morphologies because sodium citrate was used as the structure-directing agent, but an obvious impact on the crystal structure can be observed. Thus, InOOH prepared with water-ethylene glycol ratio at 30:30 was chosen in the following discussions.

Table 1. The reaction conditions for synthesizing InOOH, $In(OH)_3$ and c-In_2O_3

W:E (Volume Ratio)	60:0	50:10	40:20	30:30	20:40	10:50	0:60
Morphology	Sphere	Sphere	Sphere	Sphere	Particle	No Product	No Product
Crystal Structure	InOOH, $In(OH)_3$	InOOH, $In(OH)_3$	InOOH	InOOH	InOOH, In_2O_3	——	——

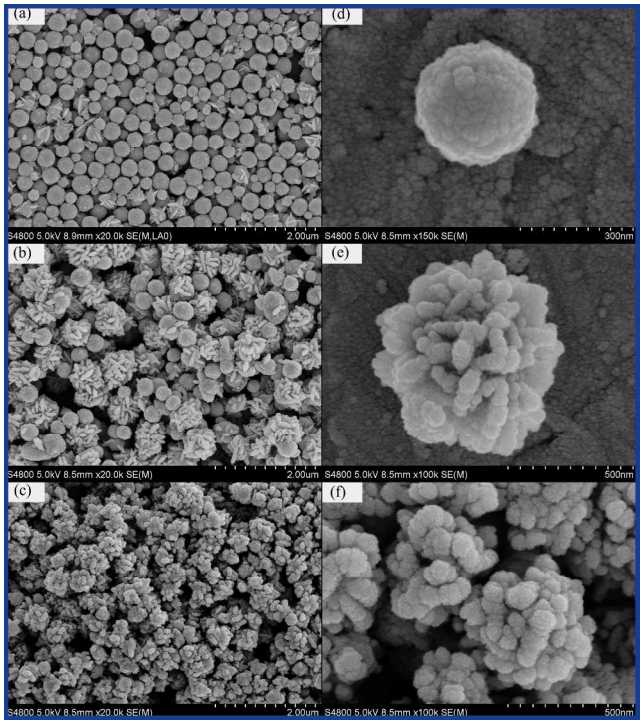

Figure 2. FESEM images of InOOH prepared at 140 °C (a, d); 160 °C (b, e); 180 °C (c, f), respectively. All the samples were synthesized at a water-ethylene glycol volume ratio of 30:30 and reaction time of 16 h.

The influence of reaction temperature on the morphology of InOOH products was investigated as well. Fig. 2a-f shows the SEM images of InOOH precursors which were synthesized at different temperatures while the water-ethylene glycol volume ratio and reaction time were kept at 30:30 and 16 h, respectively. At the reaction temperature of 140 °C, microspheres with a diameter of 250 nm could be obtained, although the morphology is not very uniform (Fig. 2a). When the reaction was carried out at 160 °C, both relatively smooth spheres and self-assembled flowers could be obtained (Fig. 2b). Similar with the porous spheres synthesized at 200 °C, these relatively smooth spheres were composed of nanoparticles in the range of several tens of nanometers, while the primary structure units of the self-assembled flowers were 2D-nanosheets (Fig. 2d&e). At the reaction temperature of 180 °C, irregular clusters with sphere-like morphology were formed (Fig. 2c&f). Only if the temperature was set at 200 °C, uniform porous spheres could be synthesized (Fig. 1c), indicating high temperature is the vital factor for the fabrication of InOOH porous spheres. It is assumed that high temperature accelerated the aggregation process thus beneficial for the formation of less packed and uniform architectures.

To understand the possible mechanism of InOOH porous spheres formation, time dependent structure evolution experiments were carried out by terminating the reaction under tap water at different time intervals. As evidenced with TEM images for these samples, crystallization time is an important factor in the formation of InOOH porous spheres. A series of TEM images (Fig. 3a-d) depicted the internal cavity evolution procedure of the porous spheres. At the initial time of 2 h (Fig. 3a), only solid microspheres with a diameter of approximate 200 nm could be obtained. With the reaction time increasing to 4h (Fig. 3b), these spheres were enlarged to around 500 nm, and the cavity started to appear because of the less packed particles. Further increasing the reaction time to 10 h leads to the gradual expansion of cavities (Fig. 3c). At this stage, the dimension of the porous spheres was quite close to the desired products. In order to verify the particle growth process, detailed size distribution histograms were presented by measuring 50 separated particles at different reaction stages, as shown in Fig. S3. Finally, uniform porous InOOH spheres could be achieved when reaction time was prolonged to 16 h or even longer (Fig. 3d).

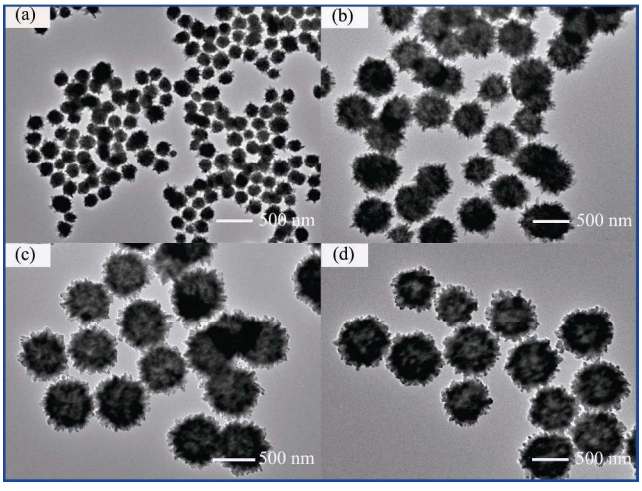

Figure 3. TEM images of the InOOH porous spheres with different reaction times: (a) 2 h; (b) 6 h; (c) 10 h; (d) 16 h, respectively. All the samples were synthesized at a water-ethylene glycol volume ratio of 30:30 and temperature of 200 °C.

In the present synthetic strategy, the hydrolysis of In^{3+} in aqueous solution leads to the formation of indium hydroxide. Because of their instability, the as-prepared indium hydroxide can dehydrate very easily at relatively higher reaction temperatures and/or in water scarcity conditions. The detailed chemical reactions are proposed as follows[17, 24]:

$In^{3+}+3OH^{-1} \longrightarrow In(OH)_3$ (Dehydration)

$In(OH)_3 \longrightarrow InOOH+H_2O$ (Dehydration)

$2InOOH \longrightarrow h\text{-}In_2O_3+H_2O$ (Calcination)

Firstly, $In(OH)_3$, InOOH, or In_2O_3 nucleus were formed at the expense of In^{3+} concentration reduction. Generally, c-In_2O_3 can be obtained via annealing the $In(OH)_3$ intermediate, while h-In_2O_3 can be achieved by annealing the InOOH precursor. It is believed that the solvent composition played an important role in the formation of indium hydroxide nucleus, thus influencing the formation of c-In_2O_3 or h-In_2O_3.

Secondly, a large number of crystallites would precipitate from solution when the concentration of crystal nucleus reached the critical limiting supersaturation point[28]. These small particles spontaneously agglomerated into spherical morphology in order to minimize their surface energy, along with the adhesion of vast structure-directing agent. It is worth mentioning that temperature could influence the packing rate thus tailor the morphologies.

Subsequently, the inside-out Ostwald ripening process play an important role in the formation of cavities[29, 30]. Nanoparticles located in the inner region are endowed with high solubility due to their larger curvatures in comparison with the particles located on the outside of the surface. Therefore, the interior particles would dissolve firstly inside and then recrystallize outside through the interparticle channels. Finally the spheres became larger while cavities were formed at the same time. The whole process was depicted in Fig. 4.

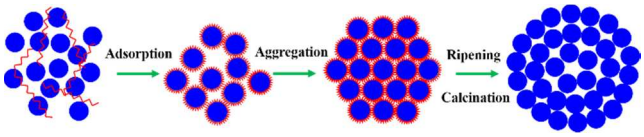

Figure. 4 Schematic diagram for the formation of h-In_2O_3 porous spheres.

Porous h-In_2O_3 spheres were obtained by annealing the as-synthesized precursor at 400 °C for 2 h. There is no doubt that InOOH is inclined to decompose with the irradiation of election beam, as well as under heat treatment conditions[26]. Here, porous h-In_2O_3 spheres with uniform size distribution were obtained under mild annealing conditions, as shown in Fig. 5a&b, the size is quite close to their InOOH precursor's, which is different from Qian's study showing that the products were subject to shrinkage after calcination[31]. In addition, the TEM images (Fig. 5c&S4b) reveal the porous feature of In_2O_3 spheres, which is retained during the post annealing process. Furthermore, the building blocks of the architectures are more detached than the precursors' and the cavities of the spheres are enlarged upon calcination (Fig. S4b). This phenomenon was attributed to the synergistic effect of the dehydration of the precursors and gas release during the surfactants removal. HRTEM images were taken (Fig. 5e) to study the fine texture of the metastable structures. Lattice spacing of 0.288 nm can be observed clearly from the HRTEM image, which corresponds to the (104) facet of h-In_2O_3. The SAED patterns (Fig. 5d) display four legible diffraction rings, which could be assigned to (012), (110), (024) and (300) diffraction planes of h-In_2O_3 with hexagonal structure. From SEM and TEM images, it can be inferred that the annealing treatment has little influence on shape and morphology, while the crystal phase was transformed from InOOH to h-In_2O_3.

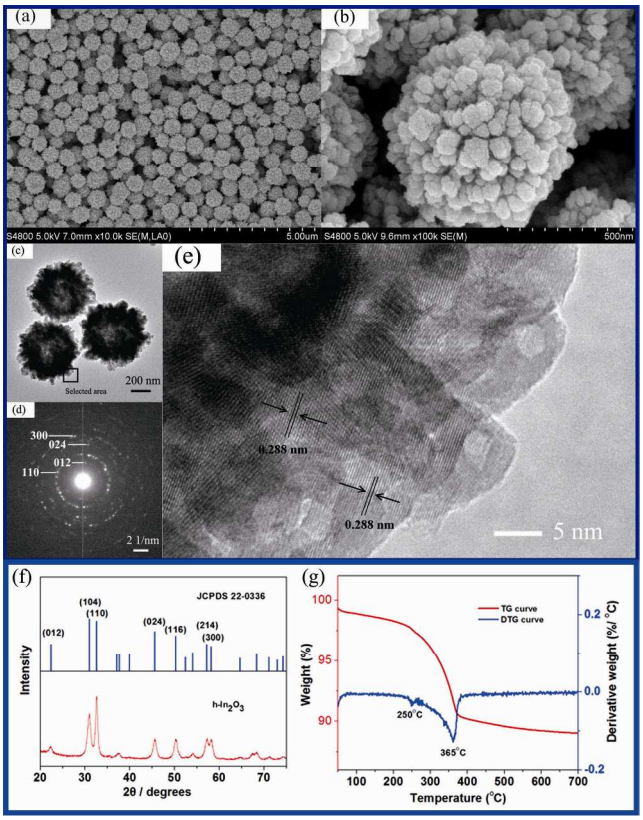

Figure. 5 (a) Low and (b) high-magnification FESEM images of h-In_2O_3 spheres; (c) low-magnification TEM images of h-In_2O_3 with (d) SAED pattern; (e) HRTEM images of h-In_2O_3 porous structures; (f) XRD patterns of h-In_2O_3 porous spheres and their corresponding JCPDS card; (g) TG and DTG curves of the obtained InOOH porous spheres. The sample was synthesized at a water-ethylene glycol volume ratio of 30:30, temperature of 200 °C and reaction time of 16 h.

X-ray diffraction was used to determine the crystallinity of the as-synthesized h-In_2O_3, as shown in Fig. 5f. All the characteristic peaks of the final products are in good agreement with h-In_2O_3 with corundum structure (JCPDS No.22-0336), confirming InOOH was completely transformed to h-In_2O_3 after annealing at 400 °C for 2 h. In order to study the evolution process from InOOH precursor to h-In_2O_3, thermogravimetric analysis was carried out. As depicted in Fig. 5g, two main steps were observed. Briefly, the first weight loss step started from environmental temperature and gradually reached 2.38 wt% at around 250 °C. This step was mainly attributed to temperature-induced desorption of water molecules from the surface of the materials. The second significant decrease appeared at 250-365 °C and this could be ascribed to chemical dehydration from InOOH to form h-In_2O_3, verified by the emergence of an evident

peak on the DTG curve. The weight change of this step is about 6.35 wt %, which is consistent with the theoretical value of 6.1 wt % within the error. On the basis of the weight loss curve, it is figured out that the h-In_2O_3 was completely formed when temperature was higher than 400 °C.

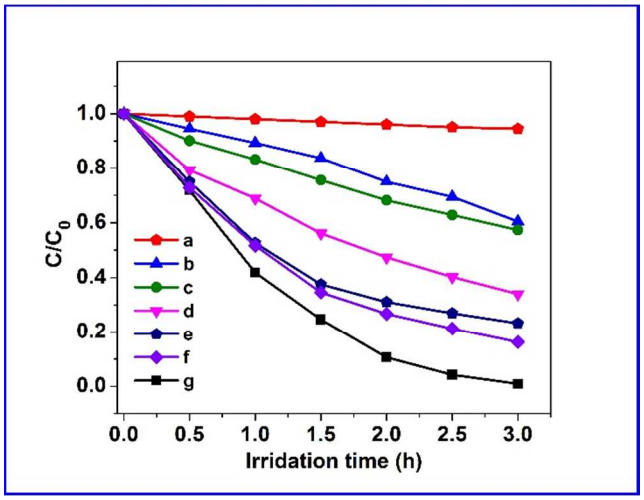

Figure. 6 Normalized degradation curves of RhB solution with (a) blank test; (b) commercial c-In_2O_3 particles; (c) h-In_2O_3 prepared at 140 °C; (d) InOOH porous spheres; (e) h-In_2O_3 prepared at 160 °C; (f) h-In_2O_3 prepared at 180 °C; (g) h-In_2O_3 porous spheres prepared at 200 °C, respectively. All the samples (c-f) were synthesized at a water-ethylene glycol volume ratio of 30:30 and reaction time of 16 h.

The photocatalytic activities of the as-synthesized h-In_2O_3 products were evaluated by degrading RhB solution under UV light irradiation. Fig. 6 shows the comparison of photocatalytic activities among the commercial c-In_2O_3 particles, InOOH porous spheres, and h-In_2O_3 products with different morphologies. In the absence of catalysts, the photolysis of RhB under UV light was almost negligible, less than 5% after irradiation for 3 h. The commercial c-In_2O_3 particles degraded nearly 40% of RhB under the same conditions. In addition, the h-In_2O_3 products synthesized at 140 °C, 160 °C, and 180 °C shows the degradation efficiency of 43%, 77%, and 84%, respectively. Before calcination, the InOOH porous spheres exhibited a moderate photocatalytic activity (degradation efficiency of 66%) in comparison with other samples. Nevertheless, approximate 99% of RhB had been degraded in the presence of h-In_2O_3 porous spheres (synthesized at water-ethylene glycol volume ratio of 30:30，temperature of 200 °C and reaction time of 16 h) at the first run. UV-Vis diffuse reflectance spectra (Fig. S5) showed the similar absorbance edge for all In_2O_3 samples, suggesting their nearly the same band gap energies[32]. Thus, the enhanced photocatalytic activity of h-In_2O_3 porous spheres was not owing to their extended visible absorption region, but their unique hierarchical structure with a relative large specific surface area, which is 18.6 m^2/g and 3 times larger than the c-In_2O_3 commercial particles (the smallest surface area of 5.15 m^2/g). This assumption could be verified by the moderate photocatalytic activity of InOOH porous spheres also. In this experiment, InOOH with the widest band gap of 3.32 eV should exhibit the lowest activity, while their performance was much higher than the commercial one. As depicted in Figure. 7a, with the increasing of irradiation time, sharp decrease of the characteristic absorption peak indicated h-In_2O_3 was very active in degradation of RhB. There is no significant blue shift of λ_{max} (554 nm) suggesting the deethylation of the conjugated chromophore structures is not the main reaction during the degradation process, most of the RhB was thoroughly degraded and mineralized into carbon dioxide and water[33].

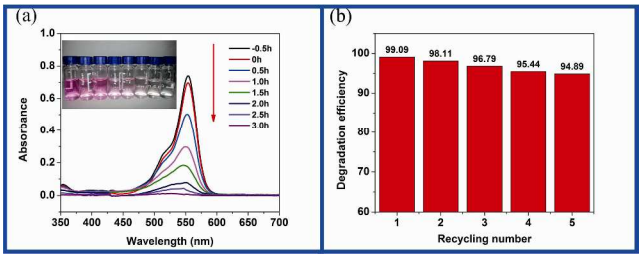

Figure.7 (a) Absorption spectra of RhB solution under UV light irradiation in the presence h-In_2O_3 porous spheres for different time intervals with their corresponding digital images inset; (b) the recycling stability histogram. The sample was synthesized at a water-ethylene glycol volume ratio of 30:30, temperature of 200 °C and reaction time of 16 h.

To investigate the recycling stability of h-In_2O_3 porous spheres, spent catalysts were collected by centrifugation for the next reaction run. Fig. 7b shows the degradation efficiency for 5 reaction runs under the same conditions. It can be verified the photocatalytic activity was decreased by 5% from 99% to 94% after 5 reaction runs. Considering the inevitable weight loss during each run, these experiment data indicate that h-In_2O_3 porous spheres possess considerable stability. Furthermore, XRD analysis and SEM images of the h-In_2O_3 photocatalysts before and after reaction were shown in Fig. 8a&b. Although the crystallinity has decreased, and some of the spheres were broken into nanoparticles, both the crystal structure and morphology could be preserved after 5 reaction circles. Apparently, the chemical stability was derived from their structural stability. Therefore, the h-In_2O_3 can be regarded as a kind of stable catalyst in the experiments.

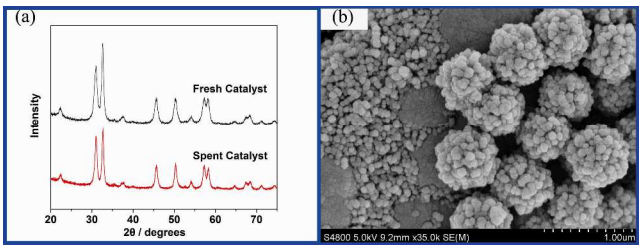

Figure. 8 XRD pattern (a) and FESEM images (b) of the h-In_2O_3 porous spheres after 5 reaction runs. The sample was synthesized at a water-ethylene glycol volume ratios of 30:30, temperature of 200 °C and reaction time of 16 h.

Conclusions

InOOH porous spheres were successfully synthesized through a facile mixed solvothermal method. The solvent composition, reaction temperature and ripening time are important factors in the orthorhombic InOOH porous spheres formation. Polycrystalline h-In_2O_3 porous spheres could be obtained after calcining their precursors at 400 °C for 2 h. Moreover, these h-In_2O_3 porous spheres exhibited excellent photocatalytic activity and stability in the degradation of RhB. Almost all the dye

degraded in less than 3 h during the first run, and the photocatalytic activity decreased slightly after 5 reaction circles, which indicates the as-synthesized h-In_2O_3 porous spheres are potential to be a powerful photocatalyst candidate for pollution treatment.

Acknowledgements

This work is financially supported by National Natural Science Foundation of China (Grant No. U 0136222 and 51271215).

Notes and references

[a] *State Key Laboratory for Heavy Oil Processing, PetroChina, Key Laboratory of Catalysis, China University of Petroleum, Qingdao 266580, China. E-mail: yzhang@upc.edu.cn, zfyancat@upc.edu.cn; Fax: +86 532 86981295; Tel: +86 15165267367, +86 532 86981296, +86 532 86981856*

[b] *Key Laboratory of Biofuels, Qingdao Institute of Bioenergy and Bioprocess Technology, Chinese Academy of Sciences, Qingdao 266101, China*

† Electronic Supplementary Information (ESI) available: [XRD patterns of the obtained samples at different water-ethylene glycol volume ratios. SEM images of the products at different water-ethylene glycol volume ratios. Low magnification SEM and TEM images of as-prepared InOOH porous spheres. The size distribution diagrams for InOOH spheres at different reaction intervals. Low magnification SEM and TEM images of h-In_2O_3 porous spheres after calcination at 400 ºC. UV-Vis diffuse reflectance spectra and plots of $(Ah\upsilon)^{1/2}$ versus $h\upsilon$ for the band gaps of different samples. XRD patterns and SEM image of the commercial c-In_2O_3 nanoparticles]. See DOI: 10.1039/b000000x/

1. A. Gurlo, *Nanoscale*, 2011, **3**, 154-165.
2. M. Willander, O. Nur, Q. Zhao, L. Yang, M. Lorenz, B. Cao, J. Z. Pérez, C. Czekalla, G. Zimmermann and M. Grundmann, *Nanotechnology*, 2009, **20**, 332001.
3. Y. Zhu, T. Ikoma, N. Hanagata and S. Kaskel, *Small*, 2010, **6**, 471-478.
4. J. Zhou, L. Gong, S. Z. Deng, J. Chen, J. C. She, N. S. Xu, R. Yang and Z. L. Wang, *Applied Physics Letters*, 2005, **87**, 223108-223108-223103.
5. J. Yu, X. Yu, B. Huang, X. Zhang and Y. Dai, *Crystal Growth and Design*, 2009, **9**, 1474-1480.
6. Z. Wang and L. Zhou, *Advanced Materials*, 2012, **24**, 1903-1911.
7. P. V. Radovanovic, C. J. Barrelet, S. Gradecak, F. Qian and C. M. Lieber, *Nano letters*, 2005, **5**, 1407-1411.
8. S.-T. Jean and Y.-C. Her, *Crystal Growth & Design*, 2010, **10**, 2104-2110.
9. M. Fang, X. Tan, B. Cheng and L. Zhang, *Journal of Materials Chemistry*, 2009, **19**, 1320-1324.
10. Y. Zheng, Y. Cheng, Y. Wang, F. Bao, L. Zhou, X. Wei, Y. Zhang and Q. Zheng, *The Journal of Physical Chemistry B*, 2006, **110**, 3093-3097.
11. R. Ostermann, D. Li, Y. Yin, J. T. McCann and Y. Xia, *Nano letters*, 2006, **6**, 1297-1302.
12. Z. Wang, D. Luan, C. M. Li, F. Su, S. Madhavi, F. Y. C. Boey and X. W. Lou, *Journal of the American Chemical Society*, 2010, **132**, 16271-16277.
13. J. Huang and L. Gao, *Crystal growth & design*, 2006, **6**, 1528-1532.
14. D. Yu, S. H. Yu, S. Zhang, J. Zuo, D. Wang and Y. Qian, *Advanced Functional Materials*, 2003, **13**, 497-501.
15. L.-Y. Chen, Z.-X. Wang and Z.-D. Zhang, *New Journal of Chemistry*, 2009, **33**, 1109-1115.
16. X. Lai, D. Wang, N. Han, J. Du, J. Li, C. Xing, Y. Chen and X. Li, *Chemistry of Materials*, 2010, **22**, 3033-3042.
17. L. Y. Chen, Y. Liang and Z. D. Zhang, *European Journal of Inorganic Chemistry*, 2009, **2009**, 903-909.
18. H. Zhu, X. Wang, F. Yang and X. Yang, *Crystal Growth and Design*, 2008, **8**, 950-956.
19. L. Y. Chen, Y. G. Zhang, W. Z. Wang and Z. D. Zhang, *European Journal of Inorganic Chemistry*, 2008, **2008**, 1445-1451.
20. R. Shannon, *Solid State Communications*, 1966, **4**, 629-630.
21. C. T. Prewitt, R. D. Shannon, D. B. Rogers and A. W. Sleight, *Inorganic Chemistry*, 1969, **8**, 1985-1993.
22. X. Wang, M. Zhang, J. Liu, T. Luo and Y. Qian, *Sensors and Actuators B: Chemical*, 2009, **137**, 103-110.
23. L. A. Pérez-Maqueda, L. Wang and E. Matijevic, *Langmuir*, 1998, **14**, 4397-4401.
24. J. Yin and H. Cao, *Inorganic Chemistry*, 2012, **51**, 6529-6536.
25. M. Hesse, H. Meier, B. Zeeh, R. Dunmur and M. Murray, *Spectroscopic methods in organic chemistry*, Thieme, 1997.
26. Z. Zhuang, Q. Peng, J. Liu, X. Wang and Y. Li, *Inorganic chemistry*, 2007, **46**, 5179-5187.
27. T. Yan, X. Wang, J. Long, H. Lin, R. Yuan, W. Dai, Z. Li and X. Fu, *New Journal of Chemistry*, 2008, **32**, 1843-1846.
28. Y. Xia, Y. Xiong, B. Lim and S. E. Skrabalak, *Angewandte Chemie International Edition*, 2009, **48**, 60-103.
29. J. Li and H. C. Zeng, *Journal of the American Chemical Society*, 2007, **129**, 15839-15847.
30. W.-S. Wang, L. Zhen, C.-Y. Xu, L. Yang and W.-Z. Shao, *The Journal of Physical Chemistry C*, 2008, **112**, 19390-19398.
31. Q. Tang, W. Zhou, W. Zhang, S. Ou, K. Jiang, W. Yu and Y. Qian, *Crystal growth & design*, 2005, **5**, 147-150.
32. P. King, T. D. Veal, F. Fuchs, C. Y. Wang, D. Payne, A. Bourlange, H. Zhang, G. R. Bell, V. Cimalla and O. Ambacher, *Physical Review B*, 2009, **79**, 205211.
33. T. Wu, G. Liu, J. Zhao, H. Hidaka and N. Serpone, *The Journal of Physical Chemistry B*, 1998, **102**, 5845-5851.